Energy Reports xxx (xxxx) xxx

Contents lists available at ScienceDirect

Energy Reports

journal homepage: www.elsevier.com/locate/egyr

Research paper

Luminescent materials as spectral converters: Power dependent profiling of solid $NaYF_4$:Yb^{3+}, Er^{3+} UCNP reveals highly efficient UVA–Blue emission

Juan M. Bujjamer [a], M. Claudia Marchi [b,c], Beatriz C. Barja [b,d,*], Hernán E. Grecco [a,c,**]

[a] Departamento de Física, Facultad de Ciencias Exactas y Naturales (FCEN), Universidad de Buenos Aires, Ciudad Universitaria (Pab. 1), Buenos Aires, C1428EHA, Argentina
[b] Departamento de Química Inorgánica, Analítica y Química Física, FCEN, Universidad de Buenos Aires, Ciudad Universitaria (Pab. 2), Buenos Aires, C1428EHA, Argentina
[c] Instituto de Física de Buenos Aires, CONICET, Ciudad Universitaria, Buenos Aires, C1428EHA, Argentina
[d] INQUIMAE-CONICET, Universidad de Buenos Aires, Ciudad Universitaria (Pab. 2), Buenos Aires, C1428EHA, Argentina

ARTICLE INFO

Article history:
Received 3 September 2019
Received in revised form 12 November 2019
Accepted 12 November 2019
Available online xxxx

Keywords:
Upconversion
Lanthanides
Nanoparticles
Energy transfer
Photophysics

ABSTRACT

Upconversion is a common process in lanthanides-based materials in which absorption of multiple low energy photons result in a high energy one. The emission spectrum is frequently tuned by changing the composition of the material. However, a commonly overlooked aspect is the non-linear power dependence which can influence the spectral and temporal properties of the emission. Moreover, as upconverting materials have been shown to increase the output current density in photovoltaic cells when used as spectral converters, the complete power profile is required to calculate the improved efficiency and needs to be incorporated in the design process.

In this work, we show that solid β-$NaYF_4$:Yb^{3+}, Er^{3+}upconversion nanoparticles, well known for the green–red emission, can also emit efficiently in the UVA–blue range. These bands are often neglected in the literature in nanosized particles despite having promising applications. In addition, we characterized their stationary and dynamic luminescence features as a function of incident power to reveal the relevant intra-band mechanisms. Our results demonstrate that the red emission at high incident power is explained by back-energy transfer. Finally, by simultaneously acquiring time resolved decays and power dependent emission slopes, we classified the spectral information to build a visual summary of the system providing a description at a glance of its complex dynamics.

1. Introduction

The process of upconversion (UC) is one of the most interesting features that lanthanide ions can offer from a photophysical standpoint (Haase and Schäfer, 2011). Given their multiple well-known equally spaced *4f* energy levels together with their long-lived excited states lifetimes (μs-ms), these ions can absorb more than one photon of the same near infrared energy in a sequential way. Such two, three and also four-fold absorption of low energy photons enables the emission of much higher energy radiation in the visible and even ultraviolet range. The difference of UC with nonlinear anti-Stokes second harmonic (SHA) or stimulated photon absorption (STPA) (Zoumi et al., 2002) processes resides on the much lower incident power densities (1 W cm^{-2} vs. 10^6 W cm^{-2}). Therefore, using UC materials enables excitation density powers comparable with those obtained by inexpensive, compact CW laser diodes or LEDs in the NIR.

Such remarkable optical properties of lanthanide-doped nanoparticles were applied during the last decade in fields as diverse as chemical sensing (Mahata et al., 2017), security (Kumar et al., 2016) and bioimaging where a deeper penetration is needed with no degradation or bleaching (Wu et al., 2009). In the last decade, these ions were incorporated in photovoltaic devices to take advantage of their unique photophysical properties with the aim to surpass the insensitivity of photovoltaic (PV) cells to the full solar spectrum which limits their conversion efficiency (Goldschmidt and Fischer, 2015). As spectral converters, these materials show huge potential to overcome fundamental non-absorption and thermalization losses found in solar panels (McKenna and Evans, 2017) as upconversion offers the potential for significant efficiency gains. Converting photons with

* Corresponding author at: INQUIMAE-CONICET, Universidad de Buenos Aires, Ciudad Universitaria (Pab. 2), Buenos Aires, C1428EHA, Argentina.
** Corresponding author at: Departamento de Física, Facultad de Ciencias Exactas y Naturales (FCEN), Universidad de Buenos Aires, Ciudad Universitaria (Pab. 1), Buenos Aires, C1428EHA, Argentina.
E-mail addresses: barja@qi.fcen.uba.ar (B.C. Barja), hgrecco@df.uba.ar (H.E. Grecco).

https://doi.org/10.1016/j.egyr.2019.11.024

Please cite this article as: J.M. Bujjamer, M.C. Marchi, B.C. Barja et al., Luminescent materials as spectral converters: Power dependent profiling of solid $NaYF_4$:Yb^{3+}, Er^{3+} UCNP reveals highly efficient UVA–Blue emission. Energy Reports (2019), https://doi.org/10.1016/j.egyr.2019.11.024.

energies below the bandgap of the active materials increases the maximum achievable of a single-junction efficiency (Shockley–Queisser limit) from 30% to 40.2% (Trupke et al., 2002). The approach, termed the third-generation solar photon conversion, involves the incorporation of a passive luminescent layer into PV cells (Shang et al., 2015).

Lanthanide-doped upconversion materials typically consist of a chemically stable dielectric host matrix doped with Ln^{3+} ions. Host materials with low phonon energy are able to produce upconversion luminescence more efficiently, as multiphonon-assisted nonradiative relaxations can be minimized. The most studied UC material is based on a hexagonal β-$NaYF_4$ matrix doped with Yb^{3+} and Er^{3+} ions. Moreover, the use of $NaYF_4$:Yb^{3+} (18%), Er^{3+} (2%) nanocrystals as upconverter in Si solar cell showed that the short circuit current density can be increased by 6.25% due to the contribution of these upconverters (De Wild et al., 2010a,b; Zhang et al., 2010).

The basic mechanism of UC (Fig. 1) involves ground and excited-state absorption (GSA–ESA), energy transfer upconversion (ETU), cooperative sensitization upconversion (CSU) and cross relaxation (CR) which can be found elsewhere (Auzel, 2004; Pollnau et al., 2000). Once that a GSA process takes place, a second photon is absorbed by ESA from the excited level 1 to level 2. ESA process occurs within a single ion and is independent of dopant concentration. ETU takes place between two neighboring ions, two activators or a sensitizer and an activator. The sensitizer absorbs the pump photons reaching level 1 and it continuously transfers the harvested photons to the excited state 1 of the activator, whereas the sensitizer relaxes back to ground state. An extra ETU process excites the activator from level 1 to level 2 from which it emits. ETU is favored at high dopant levels where the distance between ions is shorter and hence the energy transfer is more likely to occur. In CSU, two sensitizers excited ions in level 1 interact with a third ion, normally the activator ion, and cooperatively transfer their absorbed energy to excite it to a higher level 2 from which it ultimately emits. CR is also an energy transfer process between two neighbor ions: one ion transfers part of its absorbed energy in an excited level to another ion in a lower energy state. Both ions may or may not be the same type. CR is generally the UC process responsible for the concentration quenching of emission. Being a nonlinear process, UC emission spectra and decay kinetics is power dependent. However, neither the excitation density power nor the excitation source is usually described in the characterization of the stationary or dynamic emission properties of UC materials. This precludes comparing among samples of the same host and dopants obtained under different experimental conditions.

The most studied UC material is based on a $NaYF_4$ matrix doped with Yb^{3+} and Er^{3+} ions. Upon excitation of the sensitizer Yb^{3+} at 976 nm, two or more consecutive energy transfer processes excite an Er^{3+} ion to higher excited states. Subsequently, after one or more non-radiative decay steps Er^{3+} can emit green, red and blue–UVA photons. More complicated sequences of processes also contribute to the population of visible-emitting states (Anderson et al., 2014) but are still debated (Berry and May, 2015; Shin et al., 2017).

The NIR-to-Visible upconversion mechanism in the blue region was described for large micrometer β-$NaYF_4$:Yb^{3+}, Er^{3+} particles (Nadort et al., 2016), and an energy migration-mediated upconversion (EMU) was reported for nanostructures (Kaiser et al., 2017). The emission of β-$NaYF_4$:Yb^{3+}(20%), Er^{3+}(2%) UC nanometer sized particles (UCNP) dispersed in different solvents has also been described (Wilhelm, 2017) but not in solid state. When compared with their bulk counterparts, or even micrometer sized analogs, lanthanide doped UCNP often suffer from stronger surface quenching effects as a consequence of their larger surface-to-volume ratio in which surface-related effects dominate the energy-loss mechanisms. It is known that different sizes, surface conditions and crystallinity in $NaYF_4$:Yb^{3+}, Er^{3+} nanomaterials govern the different red to green emission intensity ratios and decay lifetimes (Zhao et al., 2013).

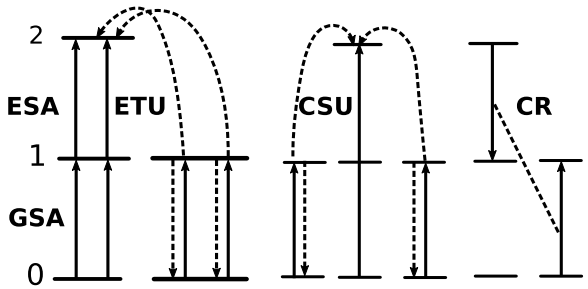

Fig. 1. Representation of the basic UC mechanisms for a three levels energy diagram. Absorption and emission are indicated by solid arrows, non-radiative decays and energy transfer processes are shown in dashed arrows.

To our surprise, detailed studies with nanometer size β-$NaYF_4$:Yb^{3+}(20%),Er^{3+}(2%) UCNP in which accurate information of the optical setup, and the role of the incident power density in the blue, green and red regions together with their in situ lifetime's measurements has not been described. In this work, we deliberately chose solid UCNP synthesized from a well-known reported method. We show that the optical properties of β-$NaYF_4$:Yb^{3+}(20%),Er^{3+}(2%) nanoparticles can be tuned by changing the excitation power, instead of the chemical composition of the samples, to produce a larger UVA and blue fractional emission without any extra dopant. We propose a characterization of the UCNP in terms of simultaneous measurements of their stationary and dynamic data to standardize the information to achieve both using it as a fingerprint of the particle and understanding their photophysics.

In this work, we show that commonly studied β-$NaYF_4$:Yb^{3+}, Er^{3+}particles can be utilized as strong emitting blue and UVA nanosized sources, apart from the previously known green and red bands, emphasizing their application in energy conversion and biologic applications. We also study them with an approach based on full lifetime and static emission characterization to explain the internal dynamics of the upconversion processes originating them.

2. Results and discussion

Stationary emission spectra: power dependence emission of the $NaYF_4$:Yb^{3+}, Er^{3+} UCNP. Upon excitation with an IR laser, the measured spectra (Fig. 2a) showed the well-known emission bands of the Er^{3+} ions in the green (G, 500–535 nm), yellow (Y, 535–570 nm) and red (R, 630–690 nm) regions as a result of the $^4S_{3/2}$, $^2H_{11/2}\rightarrow{}^4I_{15/2}$ and the $^4F_{9/2}\rightarrow{}^4I_{15/2}$ transitions, respectively. Additionally, the spectrum showed a strong dependence on the incident photon flux. Indeed, from the lowest to the highest (0.1 W cm^{-2} to 100 W cm^{-2}) incident power, we observed a wide change in emitted intensities of the whole spectrum. More interestingly, there is also a significant relative change in the emission spectra, with a 10 fold increase in the ultraviolet A (UVA, 372–390 nm) and blue (B, 397–525 nm) regions, a fact which is addressed below. These bands arise from transitions of higher levels $^2H_{9/2}\rightarrow{}^4I_{15/2}$ (410 nm) or $^4G_{11/2}\rightarrow{}^4I_{15/2}$ (383 nm) as a result of absorbing at least three IR photons. Interestingly, we found that their intensity is an order of magnitude larger than any previous report for UCNP.

The relationship between the intensity of the UC emission (I_{UC}) and the number of photons involved in the absorption mechanism can be described as: $I_{UC} = P^{\alpha}$ where α is the effective

Please cite this article as: J.M. Bujjamer, M.C. Marchi, B.C. Barja et al., Luminescent materials as spectral converters: Power dependent profiling of solid $NaYF_4$:Yb^{3+}, Er^{3+} UCNP reveals highly efficient UVA–Blue emission. Energy Reports (2019), https://doi.org/10.1016/j.egyr.2019.11.024.

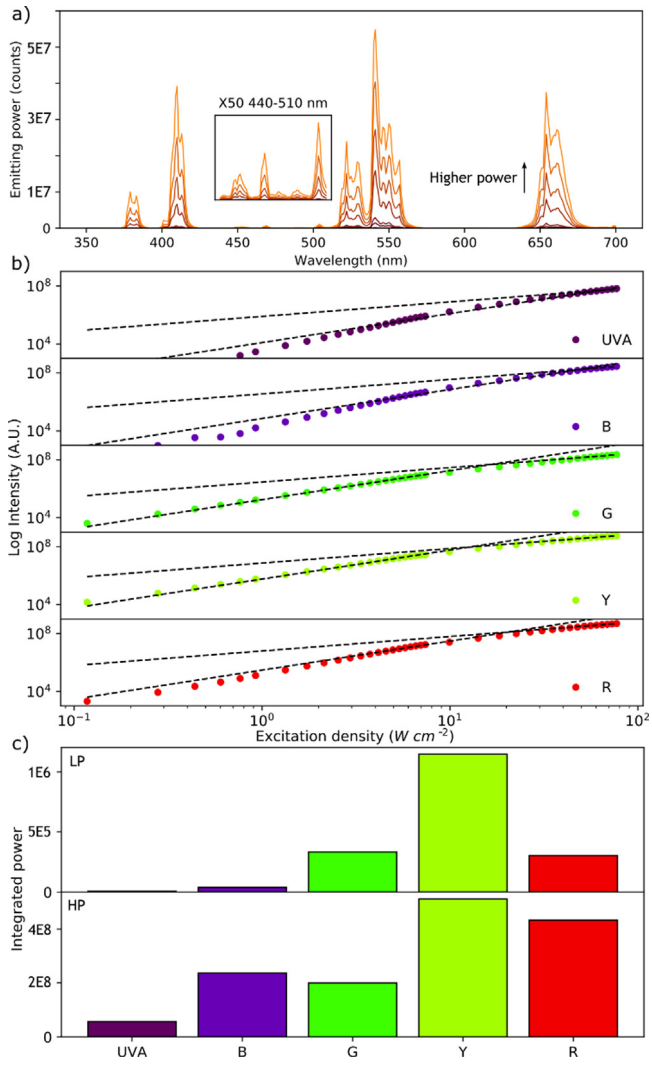

Fig. 2. Power dependent spectra emission from UVA to R ranges. (a) Emission spectra under CW 976 nm excitation for different incident power densities spanning over three orders of magnitude. Inset: magnified section of the spectrum. (b) Double logarithmic power dependence of the emission intensity vs. the incident power for a selected wavelength in each band and the limiting slopes $\alpha_1 = 2$ and $\alpha_2 = 1$ provided as a reference (dashed lines). (c) Integrated power over five different spectral bands.

number of photons involved in the absorption process per unconverted photon emitted and P is the incident power (Auzel, 2004). We fitted this model to each of the previously defined spectral bands (Fig. 2b). The change in the slope α from lower (α_1) to higher (α_2) power densities (Table 1) obeys to the different UC mechanisms involved in each case, mainly related to the way in which the intermediate levels are being populated or depopulated.

A three-photon process is necessary to generate the most (UVA-B: $\alpha_1 = 2.8$) and least (R: $\alpha_1 = 2.4$) energetic emission bands. The G and Y ranges follow a different mechanism, in which only two 976 nm photons ($\alpha_1 = 1.9$) are involved. The explanation of this behavior comes from modeling the ion's states with nonlinear dynamical equations (Pollnau et al., 2000). When excitation power remains low (the order of 1 W cm^{-2} and below), linear decay pathways dominate the depletion of a state and these have the largest slope, with a limiting value of N, the number of photons absorbed. On the other limit, is an upconverting process which starts dominating the population of the state, and these

Table 1
Emission vs. excitation limiting slopes from lower (α_1) to higher (α_2) power densities, for each spectral band.

Slope	UVA	B	G	Y	R
α_1	2.8	2.8	1.9	1.9	2.4
α_2	1.6	1.2	1.2	1.0	1.0

have slopes which are always smaller than their linear decay counterpart. In the middle zone, the curvature is explained by the relative contribution of linear decay and upconversion, having intermediate values bounded by the aforementioned limits.

To better illustrate the power dependence of the spectra we calculated the integrated area for each of the five defined emission ranges at the lowest (LP, below 1 W cm^{-2}) and highest incident (HP, more than 50 W cm^{-2}) powers (Fig. 2c). For the lowest incident power, the green–yellow emission prevails over the rest of the bands, being the blue and the UVA bands almost undetectable. On the contrary, for the highest incident power the blue and UVA emission together almost equals that of the red emission.

It is therefore clear that an increase in the incident power not only enhances the blue and UVA bands but also the red to green ratio. Out of all the UC emission mechanisms the red emission one has been the most controversial. It has been largely accepted that arises from the absorption of two 976 nm photons. These photons populate the green emitting states by GSA–ESA or GSA-ETU mechanisms after which non-radiative paths take place to the $^4F_{9/2}$ level from which red light is emitted. Lately, it has been proposed that the red UC emission involves the absorption of three, and not two, 976 nm photons. Indeed, our observations agree with this mechanism for a $NaYF_4$:Yb^{3+}, Er^{3+} host in which an intimate connection exists between NIR-to-red and NIR-to-blue upconversion process (Anderson et al., 2014; Berry and May, 2015). Our results demonstrate that the red, blue and UVA emissions involve three photon processes and are closely related to the magnitude of the incident laser power. Higher power excitations enhance the red, blue and UVA emissions to the detriment of the green bands.

In this revisited mechanism shown in Fig. 3, a ground state absorption (GSA) by the Yb^{3+} ion followed by two-step energy transfer upconversion (ETU1+ETU2) to Er^{3+}, populates the Er^{3+} ($^4F_{7/2}$) level which rapidly relaxes non radiatively to the $^2H_{11/2}$, $^4S_{3/2}$, the green emitting states. A third 976 nm photon from an ETU3 process promotes the Er^{3+} ions into higher ^4G_J (J = 7/2, 9/2, 11/2) excited states manifolds above the blue emitting $^2H_{9/2}$. After relaxing within the ^4G_J manifold, Er^{3+} can either undergo back energy transfer (BET) to Yb^{3+}, resulting in population of the Er^{3+} red-emitting state ($^4F_{9/2}$) from which it emits: $Er^{3+}(^4G_J)+Yb^{3+}(^2F_{7/2})\rightarrow Er^{3+}(^4F_{9/2})+Yb^{3+}(^2F_{5/2})$ or the $Er^{3+}(^4F_{9/2})$ can undergo multiphonon relaxation (MPR) to the blue emitting state $^2H_{9/2}$. In conclusion, both red and blue upconversion processes proceed via the same three-photon excitation mechanism being the green emitting states ($^2H_{11/2}$, $^4S_{3/2}$), the intermediate levels from which the third photon is absorbed. This mechanism for the red emission also explains the bands in the UVA range.

In order to gain further insight into the processes dominating the emission at the different wavelengths, the time resolved luminescent emission $I(t)$ was measured for each one of the previously described bands (Fig. 4). Briefly, the emission decay curves were monitored at peaking wavelengths (see Section 4). Then, by means of the recorded emission data, the mean $I(t)$ curves were calculated for the previously analyzed five different ranges (UVA, B, G, Y and R). A quick inspection of these shows at least two distinct components: an exponential decay and an exponential growth (see Fitting Models in Supporting Information

Please cite this article as: J.M. Bujjamer, M.C. Marchi, B.C. Barja et al., Luminescent materials as spectral converters: Power dependent profiling of solid $NaYF_4$:Yb^{3+}, Er^{3+} UCNP reveals highly efficient UVA–Blue emission. Energy Reports (2019), https://doi.org/10.1016/j.egyr.2019.11.024.

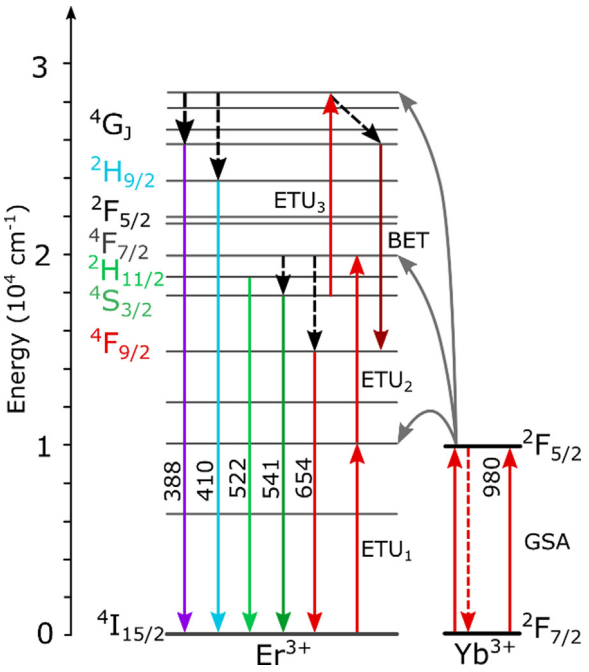

Fig. 3. Revisited mechanism of upconversion processes in $NaYF_4$: Yb^{3+}, Er^{3+} at an excitation wavelength of 976 nm including BET and different pathways for the population of the red band.

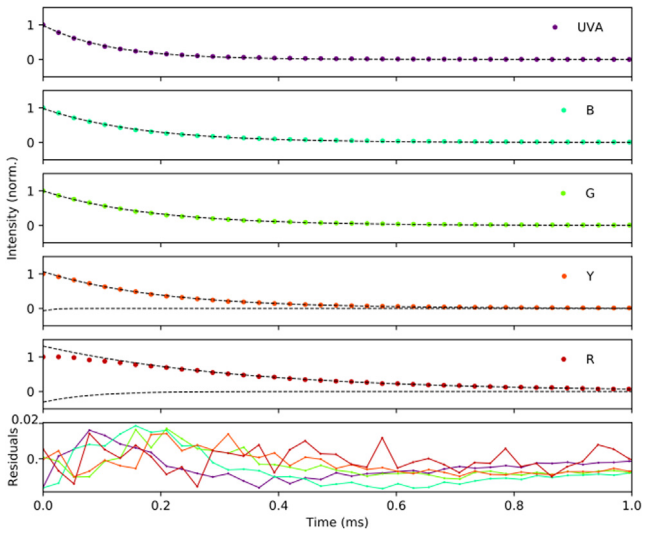

Fig. 4. Time dependent emission profiles. Normalized decay profiles for the UVA, B, G, Y and R integrated ranges at 25 W cm^{-2} of excitation power density and excitation wavelength of 976 nm. Dashed lines show the model fittings of the data points. In the bottom panel the corresponding residuals are shown.

Figure S2). Therefore, the $I(t)$ curves were modeled as a monoexponential or a biexponential decay using a statistical criterion (see Section 4).

As a general rule, shortest wavelengths decays (UVA and B) were found to be best fitted with monoexponential curves while both amplitudes are non-zero for longer wavelengths, indicating a rising time-resolved profile. This reflects the time required to populate the emitting states and reveal information about the upconversion steps prior to the emission. The fast rise component, for the green emitting states ($^2H_{11/2}$, $^4S_{3/2}$) represent the 6%–9% of the total emission intensity with lifetimes averaging 0.03 ms. For the red ($^4F_9$) emitting state, the decaying component (See Section 4) represents almost 20% of the total UC intensity (654 nm and 661 nm) with lifetimes shorter than 0.1 ms. These differences are the evidence of the distinct energy steps involved in each case.

There was no observable rise in the time profiles for the UVA and B regions ($^4G_{11/2}$, $^2H_{9/2}$) indicating that they are populated much faster than the scale under study. These higher energy levels depopulate UVA at about 0.15 ms, slightly faster than the G (0.2 ms) and twice as fast than R (0.3 ms) energy levels. Generally speaking, higher-excited states have more radiative decay pathways, explaining the increase in their total radiative rate constants. Finally, the time-resolved profiles at the shortest ranges (UVA and B) can be fitted with a monoexponential in which the amplitude of the fastest decay component (a_2) is zero.

Discrete wavelength characterization. To further analyze whether this analysis based on the spectral proximity of the peaks grouped into bands is suitable to characterize the photophysics of this type of phosphors, we performed a similar analysis for each of the measured wavelengths. To approach this objective, the power slopes and the $I(t)$ curves were calculated for each of the eighteen visible peaks.

In order to simplify data visualization, the four previously mentioned parameters ($\alpha_1, \alpha_2, \tau_1$ and τ_2) were calculated and shown in the same plot (Fig. 5a I to IV), for comparison with the averaged case (dashed line). It is worth mentioning that these averages were weighted by their respective spectral values (See Classification of peaks in Supporting information p. S2). This simple plot shows how for most bands the average scheme of a given group can explain the singular wavelength behavior, although, a few very distinct processes remain disguised or hidden by the mean characterization. The 504 nm and the 557 nm emission bands formerly considered as two-photon excitation processes, are much better explained as a three-photon ladder. The incorporation of the lifetime measurements prevents drawing the wrong conclusions from those points obscured by an average analysis.

The 541 nm value, for example, dominates the mean value because of its high spectral intensity, creating an intra G range difference, as opposed to the 504 nm case which does not fit into the averaged range. In the B region, the 469 nm case is another example where the addition of the dynamic counterpart brings further intra range discrepancies, showing in this case one transition that resembles the UVA dynamics and reveals valuable information about its decay pathways.

Stationary and dynamic measurements at a glance. As it has been shown, when a full photophysical description of UCNP is required, the information of both stationary emission spectra and excited state lifetimes at the wavelength of the most prominent bands is fundamental. Disregarding this fact, the study of the emission intensity at different incident powers is usually performed just for the strongest bands and in a short spectral range. It is of common practice to ascribe the same type of mechanism (i.e. same excitation pathway) to peaks that are in a same spectral region. Contrarily, we found that this is not the case. Indeed, the functional dependence of the weighted standardized slope α_1 against the lifetimes τ_1 for the eighteen measured wavelengths (see Static and dynamic spectral data Supporting Information p. S3) provide useful insight into the grouping of the energy transfer mechanisms (Fig. 4b). For a given wavelength, the higher the slope, the closer is the UC emission mechanism to a three-photon process. In the x-axis, longer decay components of their lifetimes are reflected in longer shifts to the right. Situations such as those observed for the 504 nm and 557 nm peaks usually termed in most papers as "green" bands do not follow a same behavior based on their static and dynamic outputs and should be distinguished for a proper characterization of the system. We

Please cite this article as: J.M. Bujjamer, M.C. Marchi, B.C. Barja et al., Luminescent materials as spectral converters: Power dependent profiling of solid $NaYF_4$:Yb^{3+}, Er^{3+} UCNP reveals highly efficient UVA–Blue emission. Energy Reports (2019), https://doi.org/10.1016/j.egyr.2019.11.024.

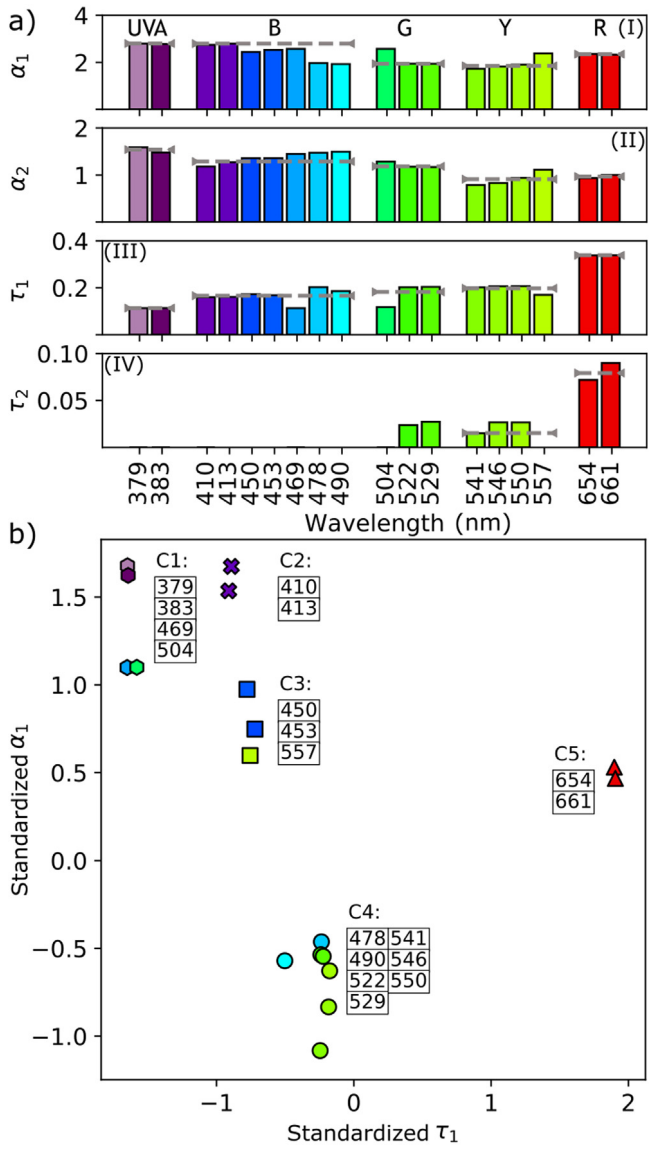

Fig. 5. (a) The two upper figures depict the values of the slopes obtained under low (α_1) or higher (α_2) incident power regimes, as discussed in the corresponding section. The lower two figures show the lifetimes τ_1 and τ_2 obtained from the decomposition of the experimental decays (see Section 4). The mean values of the α_1, α_2, τ_1 and τ_2 are represented by dashed lines for each range. b) Scatter plot of α_1 and τ_1 showing clustering among no peaks.

thus observed that both static and dynamic information of each individual band could be merged in an easy to use plot to fulfill these expectations.

Following this approach, we have implemented an automated k-means classifier to find an unsupervised partition of the spectral peaks. To this purpose, we used the same number of bands to compare them with the spectral proximity case. It is noticeable how the peaks are grouped in a distinct and more useful manner, showing clustering among wavelengths of different colors. There is no monotonic rule to map the spectral proximity with this type of clustering. These groups have the property of being less dispersed in the $\tau_1 - \alpha_1$ domain and thus expected to have more similar excitation dynamics. For example, the τ_1 axis is responsible of the large separation of the C3 and C5 groups which is not evident by just considering the α_1 dimension. It is in this way that the nontrivial behavior of a low energy region as a three-photon ladder such as the R region can be useful for a practical system characterization.

3. Conclusions

We have shown for the first time that solid $NaYF_4$:Yb^{3+}, Er^{3+} UCNP can have a strong UVA-B emission, a fact often disregarded particularly in nanosized particles having a lot of potential applications in biology and energy harvesting. While similar spectral signatures have been achieved using more complicated coatings or lanthanides combinations, making use of the nonlinearities in the photophysical systems provides an inexpensive and simple way to achieve efficient energy conversion. Non-linearities are an interesting but commonly overlooked feature as evidenced by the lack of information about excitation power density in many publications. While our excitation power density (100 W cm^{-2}) may seem high compared to the sun irradiance (10–20 W/m^2, integrated over a 30 nm band around 980 nm), usual PV topologies involve light concentration optics increasing irradiance by a factor up to 1000X (Goldschmidt and Fischer, 2015), so characterization in this range is mandatory and should be factored in for design purposes.

By profiling the emission power dependence, we demonstrated the UVA-B region of the spectra involves a three-photon process. This explains why at high excitation power it can surpass the G band which increases quadratically, but not the R regions which increases cubically. Two very distinct approaches had been shown in the past to describe these complex systems: one is multiple equation-based models and the other is an average and spectral-proximity based analysis. In the approach shown here, where a practical characterization is needed, the full stationary and lifetime measurement in the complete spectral range proved to be a valuable tool. The complexity of the decay pathways and the number of absorbed photons shows up naturally in the experimental data. This is perhaps the only information needed to separate two similarly synthesized nanosystems without neither failing to describe fundamental details of the complete process for which the full information is not always available nor oversimplifying the calculations. We found that the $\tau_1 - \alpha_1$ based metric can be used to explain some key aspects of the photophysics of the R emission and the interaction among the G and de UVA-B as a BET process evidence. This way of representing the photophysical information in a single plot offers a simple and straightforward method to get dynamic and stationary information at a glance which can be very useful in the task of selecting UCNP systems.

4. Experimental section

Synthesis of $NaYF_4$:Yb^{3+}, Er^{3+}UCNP. $NaYF_4$:Yb^{3+},Er^{3+} nanoparticles were synthesized according to a reported procedure (Zhang et al., 2012). In a typical synthesis, $YCl_3 \cdot 6H_2O$ (0.78 mmol), $YbCl_3 \cdot 6H_2O$ (0.20 mmol), $ErCl_3 \cdot 6H_2O$ (0.02 mmol) were added to a 100 mL three-necked flask containing oleic acid (6 mL) and 1-octadecene (15 mL). The solution was stirred and heated to 150 °C under vacuum for 30 min to get homogeneous solution and then cooled down to room temperature. A solution of NH_4F (4 mmol) and NaOH (2.5 mmol) dissolved in methanol (10 mL) was added under magnetic stirring to the flask and then heated slowly to 70 °C for 30 min until all the methanol evaporated. Subsequently, the solution was heated to 300 °C for 2 h under argon protection and then cooled down to room temperature. The UCNP were precipitated by adding ethanol, centrifuged and washed with hexane and ethanol three times.

Characterization. The size and morphology characterization of the sample was performed with a field emission scanning electron microscope (FESEM, Zeiss Supra 40). The UCNP were dispersed in ethanol and dropped on the surface of a silicon wafer

Please cite this article as: J.M. Bujjamer, M.C. Marchi, B.C. Barja et al., Luminescent materials as spectral converters: Power dependent profiling of solid $NaYF_4$:Yb^{3+}, Er^{3+} UCNP reveals highly efficient UVA–Blue emission. Energy Reports (2019), https://doi.org/10.1016/j.egyr.2019.11.024.

for FESEM characterization. The phase structure of as-synthesized UCNP was collected at room temperature on an X-ray powder diffractometer (Siemens D5000) with Cu K_{α} radiation ($\lambda = 1.5406$ Å) at 40 kV and 30 mA settings. Diffractogram was recorded in the 10–90° 2θ range using a step size of 0.02° and a step time of 2 s.

Morphology and structure. Synthesized $NaYF_4$:Yb^{3+}, Er^{3+} nanoparticles are hexagonal shaped prisms with uniform size distribution with 40 ± 2 nm length, 34 ± 2 nm width and 24 ± 2 nm thickness on average (Fig. 6, top panel). Oleic acid acts as a microemulsion to form microcells, which effectively limits the anisotropic growth of the UCNP (1.18 aspect ratio length:width). All the diffraction peaks can be readily indexed to those of the pure phase-hexagonal β-$NaYF_4$:Yb^{3+}(20%), Er^{3+}(2%) crystal structure (space group: $P6_3/m$) with a = 5.96 Å and c = 3.51 Å, which is in good agreement with the standard values (JCPDS No. 28-1198, Fig. 6, bottom panel). No other impurity peaks can be detected, which indicates that the nanocrystals are single-phased. The crystallite size estimated by line-broadening is 18 nm using Debye–Scherrer equation to (201) peak.

Stationary emission measurements. Spectral measurements were acquired with a spectrofluorometer (Horiba PTI QuantaMaster) equipped with a photomultiplier tube (PMT). Briefly, a 976 nm and 300 mW fiber coupled laser diode (Thorlabs BL976-SAG300) was focused into the sample to provide larger power density. In addition, a neutral filter was used in order to further increase the dynamic range of the excitation power. Monochromator slits were set in order to have a suitable peak resolution matched with a step size of 1 nm. Emission wavelength sweep was in the 350–700 nm range. The powders were supported inside quartz windows and measured as such at room temperature in a front face arrangement to minimize the collection of stray light. (see Experimental Setup in Supporting Information p. S4).

Time-dependent emission measurements. To perform dynamic measurements a photon counting system was coupled to the conformed pulse output of the previously described spectrofluorometer. The counting mechanism was implemented with a FPGA microcomputer as an analog acquisition system (Red Pitaya 125-14). We used less than 5% of the maximum bandwidth of the detector to avoid pulse pile-up effect. The sample was excited using a square laser pulse with characteristic times longer than the population and depopulation ones. Measurements were performed with a 1 nm resolved window for the centered at the whole set of eighteen peaks: 379 nm, 383 nm, 410 nm, 413 nm, 450 nm, 453 nm, 469 nm, 478 nm, 490 nm, 504 nm, 522 nm, 529 nm, 541 nm, 546 nm, 550 nm, 557 nm, 654 nm and 661 nm. The stationary and dynamic measurements were performed always in situ and on the same sample.

Fitting of time-dependent measurements. Dynamic data was fitted with the biexponential mode $a_1e^{-t/\tau_1} - a_2e^{-t/\tau_2}$. Bayesian criterion for the quality of fit tests (see Fitting Models in Supporting Information p. S1) were performed over the complete dataset in order to assess the validity of the decay model with a p-value of 0.05. All cases were checked against both, the simpler monoexponential model a_1e^{-t/τ_1} and the more complex, three component model $a_1e^{-t/\tau_1} - a_2e^{-t/\tau_2} - a_3e^{-t/\tau_3}$. For all peaks, the model minimizing the Bayesian metric was kept. The analysis was revalidated according to the Akaike and Fisher F-test criteria yielding the same results. On the other hand, models with one biexponential prefactor component less than 5% smaller than the other were treated as monoexponentials for the sake of uniformity.

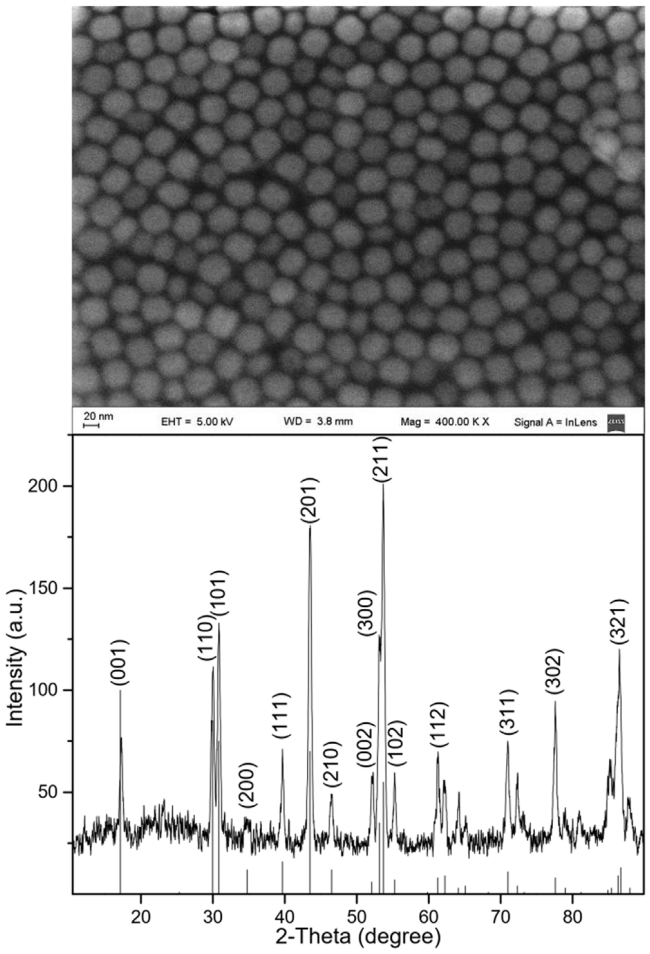

Fig. 6. $NaYF_4$:Yb^{3+}(20%),Er^{3+}(2%) UCNP morphology and structure. (Top) SEM images showing hexagonal shaped prism, (bottom) XRD powder pattern for UCNP synthesized at 300 °C and line pattern of the standard data of hexagonal β-$NaYF_4$:Yb^{3+}, Er^{3+} are given as reference.

Declaration of competing interest

The authors declare that they have no known competing financial interests or personal relationships that could have appeared to influence the work reported in this paper.

Acknowledgments

We acknowledge UBA (20020130200271BA), FAN (PreSemillas) and ANPCyT (PICT-2013-1301) for funding the present project.

Appendix A. Supplementary data

Supplementary material related to this article can be found online at https://doi.org/10.1016/j.egyr.2019.11.024.

References

Anderson, R.B., Smith, S.J., May, P.S., Berry, M.T., 2014. J. Phys. Chem. Lett. 5, 36–42.
Auzel, F., 2004. Chem. Rev. 104, 139–174.
Berry, M.T., May, P.S., 2015. J. Phys. Chem. A 119, 9805–9811.
De Wild, J., Meijerink, A., Rath, J.K., Van Sark, W.G.J.H.M., Schropp, R.E.I., 2010a. Sol. Energy Mater. Sol. Cells 94, 1919–1922.
De Wild, J., Rath, J.K., Meijerink, A., Van Sark, W.G.J.H.M., Schropp, R.E.I., 2010b. Sol. Energy Mater. Sol. Cells 94, 2395–2398.
Goldschmidt, J.C., Fischer, S., 2015. Adv. Opt. Mater. 3, 510–535.

Haase, M., Schäfer, H., 2011. Angew. Chem., Int. Ed. 50, 5808–5829.
Kaiser, M., Würth, C., Kraft, M., Hyppänen, I., Soukka, T., Resch-Genger, U., 2017. Nanoscale 9, 10051–10058.
Kumar, P., Singh, S., Gupta, B.K., 2016. Nanoscale 8, 14297–14340.
Mahata, M., Bae, H., Lee, K., 2017. Molecules 22, 2064.
McKenna, B., Evans, R.C., 2017. Adv. Mater. 29, 1606491.
Nadort, A., Zhao, J., Goldys, E.M., 2016. Nanoscale 8, 13099–13130.
Pollnau, M., Gamelin, D.R., Lüthi, S.R., Güdel, H.U., Hehlen, M.P., 2000. Phys. Rev. B 61, 3337–3346.
Shang, Y., Hao, S., Yang, C., Chen, G., 2015. Nanomaterials 5, 1782–1809.
Shin, K., Jung, T., Lee, E., Lee, G., Goh, Y., Heo, J., Jung, M., Jo, E.-J., Lee, H., Kim, M.-G., et al., 2017. Phys. Chem. Chem. Phys. 19, 9739–9744.
Trupke, T., Green, M.A., Würfel, P., 2002. J. Appl. Phys. 92, 4117–4122.
Wilhelm, S., 2017. ACS Nano 11, 10644–10653.
Wu, S., Han, G., Milliron, D.J., Aloni, S., Altoe, V., Talapin, D.V., Cohen, B.E., Schuck, P.J., 2009. Proc. Natl. Acad. Sci. 106, 10917–10921.
Zhang, X.D., Jin, X., Wang, D.F., Xiong, S.Z., Geng, X.H., Zhao, Y., 2010. Phys. Status Solidi Curr. Top. Solid State Phys. 1128–1131.
Zhang, J., Li, B., Zhang, L., Jiang, H., 2012. Chem. Commun. 48, 4860.
Zhao, J., Lu, Z., Yin, Y., McRae, C., a Piper, J., Dawes, J.M., Jin, D., Goldys, E.M., 2013. Nanoscale 5, 944–952.
Zoumi, A., Yeh, A., Tromberg, B.J., 2002. Proc. Natl. Acad. Sci. USA 99, 11014–11019.

Please cite this article as: J.M. Bujjamer, M.C. Marchi, B.C. Barja et al., Luminescent materials as spectral converters: Power dependent profiling of solid $NaYF_4:Yb^{3+}$, Er^{3+} UCNP reveals highly efficient UVA–Blue emission. Energy Reports (2019), https://doi.org/10.1016/j.egyr.2019.11.024.